Synthetic Aperture Techniques with a Virtual Source Element

Catherine H. Frazier, *Student Member, IEEE*, and William D. O'Brien, Jr., *Fellow, IEEE*

***Abstract*—A new imaging technique has been proposed that combines conventional B-mode and synthetic aperture imaging techniques to overcome the limited depth of field for a highly focused transducer. The new technique improves lateral resolution beyond the focus of the transducer by considering the focus a virtual element and applying synthetic aperture focusing techniques. In this paper, the use of the focus as a virtual element is examined, considering the issues that are of concern when imaging with an array of actual elements: the tradeoff between lateral resolution and sidelobe level, the tradeoff between system complexity (channel count/amount of computation) and the appearance of grating lobes, and the issue of signal to noise ratio (SNR) of the processed image. To examine these issues, pulse-echo RF signals were collected for a tungsten wire in degassed water, monofilament nylon wires in a tissue-mimicking phantom, and cyst targets in the phantom. Results show apodization lowers the sidelobes, but only at the expense of lateral resolution, as is the case for classical synthetic aperture imaging. Grating lobes are not significant until spatial sampling is more than one wavelength, when the beam is not steered. Resolution comparable to the resolution at the transducer focus can be achieved beyond the focal region while obtaining an acceptable SNR. Specifically, for a 15-MHz focused transducer, the 6-dB beamwidth at the focus is 157 μm, and with synthetic aperture processing the 6-dB beamwidths at 3, 5, and 7 mm beyond the focus are 189 μm, 184 μm, and 215 μm, respectively. The image SNR is 38.6 dB when the wire is at the focus, and it is 32.8 dB, 35.3 dB, and 38.1 dB after synthetic aperture processing when the wire is 3, 5, and 7 mm beyond the focus, respectively. With these experiments, the virtual source has been shown to exhibit the same behavior as an actual transducer element in response to synthetic aperture processing techniques.**

I. Introduction

A basic limitation of conventional B-mode imaging is that lateral resolution depends on the depth in the image. The best resolution is achieved only for the slice of the image containing echoes from the focus of the transducer. Passman and Ermert [1] introduced a technique to overcome this resolution limitation. The new technique involves treating the focus of the transducer as a virtual source for synthetic aperture (SA) processing. In their formulation, the virtual source is assumed to produce approximately spherical waves over a certain aperture angle. They consider the transmit signal in detail, transmitting different signals for each depth and prefiltering with a pseudoinverse filter to compensate for the attenuation of the tissue. These steps are used in an attempt to achieve depth-independent resolution at frequencies up to 250 MHz. The work reported herein extends previous work with virtual sources by examining more fundamental issues such as lateral resolution, sidelobe levels, spatial sampling rate, and SNR for images created at lower frequencies. This work studies the model for a virtual source and examines images produced with data from virtual sources, processed using known techniques to improve SA images.

Apodization weights are commonly applied to signals from individual array elements in order to reduce the sidelobe level of the beam pattern. However, these weights also have the effect of increasing the main lobe width, degrading the lateral resolution of the image. This tradeoff between sidelobe level and resolution is studied by looking at the resolution of wire targets in water and in a tissue-mimicking phantom, and by looking at the contrast resolution of cyst targets in images formed using different apodization weighting functions. It will be shown that, the boxcar weights produce the best lateral resolution and that the Hamming weights do not produce the image with the lowest sidelobes, even though the Hamming weights have the lowest sidelobes of the four weighting functions used in this study. Cosine or triangle weighting functions produce a compromise between good lateral resolution and low sidelobe level.

In addition, the formation of grating lobes, which appear if the array is undersampled, is a concern when doing SA imaging. When imaging with an array of elements, the spatial sampling is limited by the physical size of the elements, the required separation of the elements to prevent crosstalk, and the complexity added to the system by having more channels. With an array of virtual sources, it is preferable to keep the sampling rate low to reduce the amount of computation. When the beam is not steered, grating lobes can appear if the elements are spaced more than half a wavelength apart; however, it will be shown that the amplitude of these grating lobes may not be significant until the spatial sampling is much greater.

SNR is studied to analyze whether or not it can be acceptable for images created with virtual sources. It will be shown that, for targets beyond the focus of the transducer, images created through SA processing have an SNR that is improved compared to conventional B-mode imaging. And the SNR of these images is comparable to conventional B-mode images of targets that are at the focus of the transducer.

Manuscript received February 25, 1997; accepted August 11, 1997. This work was supported by NSF Fellowship (CHF) and U.S. Army contract (DACA88-94-D0008).

The authors are with the Bioacoustics Research Laboratory, Department of Electrical and Computer Engineering, University of Illinois, Urbana, IL 61801 (e-mail: wdo@uiuc.edu).

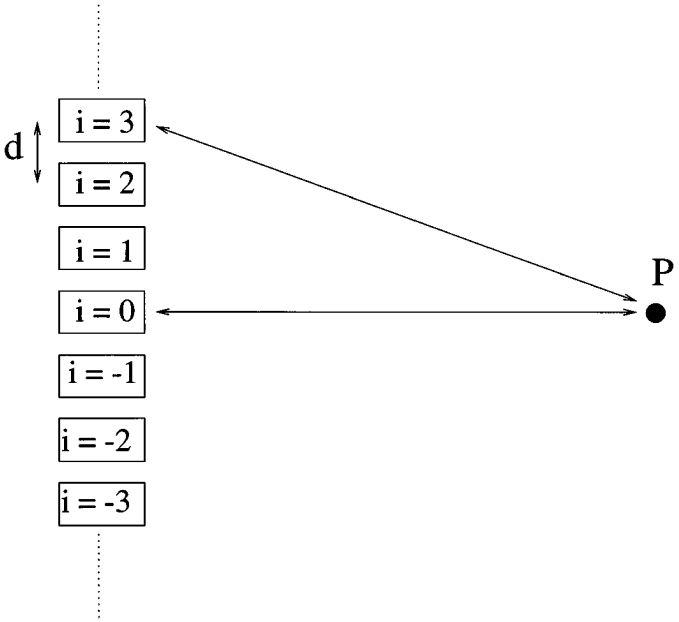

Fig. 1. Geometry of focusing situation. Elements are numbered such that the zeroth element is the center element of the subaperture. P is the desired focal point and d is the interelement distance.

II. Synthetic Aperture Imaging

Delay-and-sum beamforming uses the appropriate delay of received signals to achieve focusing. Because off-line processing is used, the delays are actually implemented as appropriate advances of some received signals.

A portion of the array is shown in Fig. 1. It is desired to focus at a point P that is located in the far field of the individual elements and in the transition region of the subaperture of the array. The field from the subaperture will be focused at P if the pulses from all the elements arrive simultaneously at P, which is achieved by advancing the signals from the elements away from the center of the subaperture and then summing the received signals from all the elements in the subaperture. Simply using the Pythagorean theorem to find the pathlength for an element i, the amount of the advance should be:

$$\Delta t_i = \frac{2z}{c}\left(1 - \sqrt{1 + \frac{(id)^2}{z^2}}\right) \tag{1}$$

where Δt_i is the time delay for element i, z is the distance to the desired focal point from the center of the subaperture, c is the speed of sound, and d is the interelement spacing. Then beamforming is accomplished with the following sum:

$$A(t) = \sum_i w_i S_i(t - \Delta t_i) \tag{2}$$

where $A(t)$ is the computed RF echo return, and w_i is a weight assigned to the returned signal, $S(t)$, from element i.

The number of signals included in the sum of (2) is determined by the aperture angle of the transducer beam beyond the transducer's focus. The beam spread of a source is determined by the geometry of the source and the wavelength of sound in the medium, which will be described in more detail in the next section.

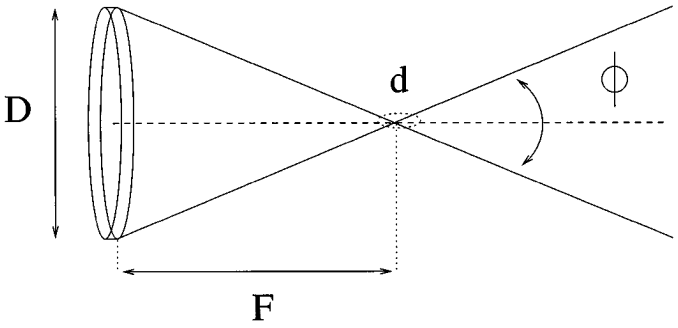

Fig. 2. Parameters that describe transducer beam. D is the transducer diameter, F is the focal length, d is the diameter of the focal spot, and ϕ is the aperture angle.

III. Issues in Synthetic Aperture Imaging

A. Model for Virtual Element

We model the virtual element as a source of spherical waves over a certain aperture angle. This model is verified by Passman and Ermert [1] through the derivation of the diffraction-impulse-response (equation 8 in [1]). A more complete derivation of this impulse response is found in [2], where the transverse field pattern is shown to vary with the type of excitation (transient or sinusoidal) and for transient excitation, with the type of detection used (positive peak or negative peak). For this study, the beam pattern after the focus of the transducer is simulated and measured for a 15-MHz transducer with an f-number of 1.5 using a technique introduced by Raum and O'Brien [3].

In a simple approximation, the initial beam spread after the focus will look like the reverse of the beam narrowing before the focus, and the degree of spreading is approximately equal to the degree of focusing before the spot as shown in Fig. 2. The half angle at which the beam spreads can be approximated by $\frac{\phi}{2} = \tan^{-1}\frac{D}{2F}$, where ϕ is the angle of spreading measured between nulls, F is the focal distance, and D is the diameter of the focused transducer. By this formulation, the virtual source of the 15-MHz transducer used in this experiment has an aperture angle of 36.9 degrees. The virtual source for the 20-MHz transducer has an aperture angle of 28.1 degrees. It is this aperture angle that determines the number of elements included in the sum in (2).

When imaging with a single focused transducer (conventional imaging), lateral resolution is inversely proportional to the aperture size; therefore, a large diameter transducer is preferred. In SA imaging, it is desirable to have a small transducer element to achieve good lateral resolution. SA imaging techniques use a small aperture transducer element to sample the large aperture, and then

TABLE I
TIME DOMAIN AND FREQUENCY DOMAIN WINDOW CHARACTERISTICS FOR LENGTH-M WINDOWS.

Characteristics for Length-M Windows			
Window	Time domain description	Main lobe width	Peak sidelobe (dB)
boxcar	1	$\frac{4\pi}{M}$	−13
cosine	$\cos\left(\frac{\pi}{2}\frac{n-\frac{M-1}{2}}{\frac{M-1}{2}}\right)$	$\frac{20\pi}{3M}$	−23
triangle	$1-\left\lvert\frac{2(n-\frac{M-1}{2})}{M-1}\right\rvert$	$\frac{8\pi}{M}$	−27
Hamming	$0.54-0.46\cos\frac{2\pi n}{M-1}$	$\frac{8\pi}{M}$	−43

the received signals from the elements are summed as in (2) with time delays to synthesize the received signal from a large focused transducer. The image SNR is maximized by including in the sum all the elements whose beams encompass the desired focal point, and excluding all other elements. If each element has a narrow beam, then only a few will have beams that illuminate the desired focal point and only those few will be included in the sum. The synthesized aperture will be small, which means that the synthesized aperture cannot achieve good lateral resolution. On the other hand, if each element has a wide beam, then the returned signals from more elements can be included in the sum, and the sampled aperture, which includes more elements, will be larger. In the case of virtual sources, the more highly focused the transducer, the better resolution will be achieved through synthetic aperture processing.

B. Reduction of Sidelobes

The tradeoff between resolution and peak sidelobe level is examined in this study. In array imaging, weighting the individual elements is known as apodization. Apodization may occur on transmit or receive; however, apodization on transmit would mean that, in some cases, a lower amplitude signal is transmitted, reducing the signal to noise ratio. Also, for monostatic data collection, where a single transducer is used for transmit and receive, the signal from one position is used several times, with different weights in different windows. Apodization on transmit would require several transmits from the same transducer position to get the signals at the appropriate weights for the different focusing positions. Therefore, in this study, apodization weights are applied in receive. In signal processing, apodization is called windowing. Signal processing theory shows that the windowing operation broadens the main lobe and lowers the sidelobes [4].

Several windows are used for this study. They are the boxcar, triangle, cosine, and Hamming windows. Characteristics of these windows are shown in Table I. From these descriptions, we expect the boxcar window to produce the image of the wire with the best lateral resolution and the Hamming window to produce the image with the lowest sidelobes. In fact, the Hamming window will not produce the image with the lowest sidelobes because apodization weights are applied only on receive; the transmit weights are always the boxcar weights. The overall beam pattern is the product of the transmit and receive beam patterns. For the cosine, triangle, and Hamming windows, the first sidelobe of the boxcar window (used on transmit) falls within the main lobe of the their beam patterns. Taking the product of the two beam patterns means that the first sidelobe of the overall pattern will be at the location of the first boxcar sidelobe with slightly reduced amplitude. The reduction in amplitude depends on how fast the main lobe falls off. As the main lobe width increases, that first boxcar sidelobe is closer to the central high part of the main lobe. Therefore, as the main lobe of the receive beam pattern widens, the expected sidelobe level of the overall beam pattern increases.

The apodization weights will also have an effect on the images of cyst targets. Even though both cysts and wire targets represent large impedance mismatches for the ultrasound signal, wire targets are more easily distinguished in an image. When the main lobe is over the cyst, there are sidelobes over regions that reflect sound. The signal reflected by the sidelobes appears to have been reflected from inside the cyst. The ability to differentiate a cyst from the surrounding medium is called contrast resolution. By reducing the main lobe width or lowering the sidelobes, contrast resolution can be improved.

C. Eliminating Grating Lobes

We also examine the effects of spatial sampling of the array of virtual sources on the appearance of grating lobes. To eliminate grating lobes, the aperture should be sampled adequately. It has been shown in [5] that, for an array of simple sources used in transmission and reception, with one active element and no beam steering, the array must have elements spaced no greater than $\frac{\lambda}{2}$ apart to prevent the formation of grating lobes. This fact can be seen from the array factor:

$$H_A(\theta)=\frac{1}{N}\frac{\sin(Nkd\sin\theta)}{\sin(kd\sin\theta)} \tag{3}$$

where N is the number of elements in the sum, k is the wave number, d is the interelement spacing, and θ is the azimuth direction. Both the numerator and denominator go to zero when $kd\sin(\theta)$ is an integer multiple of π, as expressed in (4):

$$kd\sin(\theta)=m\pi \tag{4}$$

$$\sin(\theta)=\frac{\lambda}{2\pi}\frac{1}{\mathrm{d}}m\pi \tag{5}$$

$$\sin(\theta)=\frac{\mathrm{m}\lambda}{2\mathrm{d}}\ \text{for m}=0,\,1\ \cdots\left\lfloor\frac{2\mathrm{d}}{\lambda}\right\rfloor. \tag{6}$$

Maxima in the beam pattern occur in directions described by (6). To eliminate grating lobes, the interelement spacing, d, should be made slightly smaller than half a wavelength. No effects of steering the array are considered in

this discussion because steering is not used in any processing in this paper. It can be shown that, if the beam is to be steered −90 to +90 degrees, the distance between elements should not be greater than a quarter of a wavelength [6].

The above analysis shows the directions where grating lobes occur. With a more detailed approach, the amplitude of the grating lobes will be seen to be lower than the amplitude of the main lobe [5]. First, for a real source, the output of the transducer element is limited in direction. Not all the elements will be able to contribute to the beam pattern at all angles. Therefore, the beam pattern of the array will be the product of the array factor in (3) and a modulating factor which is the angular response from an individual element. This fact is a result of the Fourier transform property of the far-field pattern. The angular response of a focused transducer is complicated. As simulated for the 15-MHz transducer, beyond the focus and close to the beam axis, the pressure amplitude oscillates. Beyond approximately 10 degrees from the beam axis (where the coordinate origin is at the focus), the pressure amplitude decreases. This modulating factor will reduce the amplitude of grating lobes at all angles beyond 10 degrees.

Second, in the above analysis, the transmitted signal is assumed to be a continuous wave. Suppose the transmitted signal is a gated sinusoid of m cycles. The pulses from all the elements will sum in phase at the location of the main lobe because the path lengths are all equal. However, at the first grating lobe location, the pulses from only m elements add in phase. The pulse from the $m+1$ element will not overlap with the pulse from the first element because they have been separated in time. This reduces the amplitude of the grating lobe by a factor of $20 \log \frac{M}{m}$ where M is the number of signals that contribute to the main lobe and m is the number of cycles in the pulse.

Third, if the transmitted pulse is a burst created by exciting the transducer with a voltage spike rather than a gated sinusoid, the grating lobes are further reduced in amplitude. The lengths of the pulse that overlap at grating lobe locations will not match exactly as they would for the sinusoidal excitation. The combination of all these effects may reduce grating lobes to a level comparable to sidelobes or lower depending on the spatial sampling.

IV. Data Collection

A schematic of the data acquisition system is shown in Fig. 3. The system uses of a host PC (ZEOS 66 MHz 486) to control a five-axis (three translational, two rotational) precision positioning system with a positional accuracy of 2 μm (Daedal, Inc., Harrison City, PA) and to retrieve waves from a digital oscilloscope. After the transducer has been manually positioned, one translational axis is used for the scan. A Panametrics (Waltham, MA) Model 5800 pulser-receiver in pulse/echo mode is used to generate the 300 V monocycle pulse which excites the transducer. The received signal is amplified (40 dB), bandpass filtered (1–35 MHz), and then displayed on either a Tektronix 11401

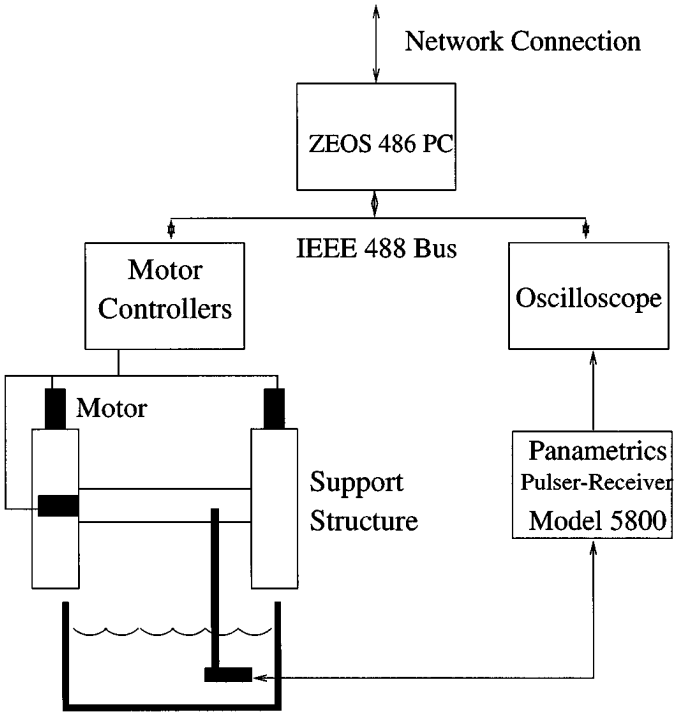

Fig. 3. Schematic of data collection system.

(Pittsfield, MA) or a LeCroy 9374L (Chestnut Ridge, NY) digitizing oscilloscope. The PC retrieves the digitized RF waveforms from the oscilloscope via IEEE-488 communications and stores them. Then the waveforms are transferred via ftp to a SUN Sparc 20 for processing.

Two Panametrics transducers with different focusing characteristics but with focal points of similar size are used to collect the data for this study. The 15-MHz transducer has a 12.7-mm diameter circular aperture and a reported 19.1-mm focal distance. The 20-MHz transducer has a 6.35-mm diameter circular aperture and a 12.7-mm focal distance. Thus, the quantity $\frac{\lambda F}{D}$ for each transducer is 150 μm, where F is the focal distance and D is the diameter. The 15-MHz transducer has a measured aperture angle of 42 degrees; the calculated aperture angle is 36.9 degrees. The 20-MHz transducer has a measured aperture angle of 33 degrees; the calculated aperture angle is 28.1 degrees.

Several data sets are created with a 25-μm tungsten wire target in degassed water. Lateral scans are made using each transducer, with the tungsten wire target positioned at the focus and at 3, 5, and 7 mm beyond the focus of the transducer. The pulse-echo RF data are collected 50 μm and 35 μm apart for the 15-MHz and 20-MHz transducers, respectively. The sampling rate is 500 MHz for the wire positioned at 7 mm and 1 GHz for all other wire positions. These data are used for measurements of resolution, sidelobe level, and SNR. One data set is collected with the 15-MHz transducer with the wire at 8 mm beyond the focus where pulse-echo RF returns are collected 20 μm apart and the temporal sampling rate is 500 MHz. This set is used for experiments with spatial sampling.

Two other sets of RF data are acquired using a tissue-mimicking phantom. These data sets are collected with the 15-MHz transducer positioned such that the signal of interest is not hidden in the reflection from the surface of the phantom. One data set uses embedded wires as the targets. These pulse-echo returns are collected 100 μm apart with a temporal sampling rate of 250 MHz. The second set uses anechoic regions as the targets. Those pulse-echo returns are collected at positions 50 μm apart with a temporal sampling rate of 200 MHz.

The phantom (Model 539, ATS Laboratories, Inc., Bridgeport, CT) is made of urethane rubber with a speed of sound of 1450 m/s at room temperature and an attenuation of 0.5 dB/cm/MHz. The embedded wire targets are made of monofilament nylon with a 0.12-mm diameter. The deepest wire in the images is positioned 1 cm below the phantom surface. The other three wires are each 1 mm closer to the surface and 5 mm to the side of the neighboring wire. The cyst targets are anechoic regions 2 and 3 mm in diameter, both positioned such that their centers are 1 cm beneath the surface of the phantom.

Ideally, to create a high resolution image, SA processing should proceed in two lateral dimensions. Collecting data using a lateral scan in one direction perpendicular to the orientation of a wire target effectively converts the problem to two dimensions.

In this study, a C program is used to perform delay-and-sum beamforming with various apodization weights. In this processing, the position of the virtual source is assumed to coincide with the position of the focus as reported by Panametrics. Measurements confirm this to within 350 μm for the 15-MHz transducer and within 260 μm for the 20-MHz transducer [3]. After this processing, the data are transferred to Matlab (The MathWorks, Inc., Natick, MA) to produce an image and determine the beamwidths, sidelobe levels, CNR, and SNR. The images are produced by bandpass filtering the RF data, envelope detection, logarithmic compression, and then displaying the data over a 50-dB range.

V. Results and Discussion

A. Resolution versus Sidelobe Level

The tradeoff between resolution and sidelobe level through the application of apodization weights is explored using tungsten wires in a waterbath, and nylon wires and cyst targets in a tissue-mimicking phantom. Numerical values of 6-dB transmit-receive beamwidth and sidelobe level for each transducer, tungsten wire depth, and window are given in Table II. The processed images show improvement in both resolution and sidelobe level compared to the unprocessed raw data. After processing, the resolution of the wires at 3 mm and 5 mm and only slightly larger than the resolution achieved at the focus of the transducers, which is 157 μm for the 15-MHz transducer and 159 μm for the 20-MHz transducer. Although the resolution should be independent of depth, the resolution of the wire at 7 mm is worse than for the two more shallow wires.

An improvement in sidelobe levels is observed. The expected sidelobe levels result from the product of the transmit beam pattern and the receive beam pattern. When the boxcar window weights are used on receive, the expected sidelobe level is -26.5 dB, or twice the sidelobe level of the weights applied once. The expected sidelobe levels are -30.0 dB, -27.0 dB, and -26.5 dB for the cosine, triangle, and Hamming weights, respectively. The obtained results are close to the expected results except for the 3 mm wire position for the 15-MHz transducer, where the sidelobe level is lower, and the 7 mm wire position for the 20-MHz transducer, where the sidelobe level is higher than expected.

Typical tungsten wire images created by this technique are shown in Fig. 4. The boxcar window produces the images with the best lateral resolution for all the depths; however, the sidelobes are also the highest for all the depths compared to the other windows. The Hamming window produces the images with the worst lateral resolution, but the sidelobe levels are not correspondingly lower than for the other windows. Images produced with the cosine window have slightly better resolution than those produced with the triangle window, although the performance of these two windows is comparable.

Fig. 5 plots the beamwidth of the main lobe versus depth with and without SA focusing using the boxcar window. The difference in the plots for no processing and with processing shows the improvement in resolution that can be achieved by applying this technique. Ideally, with SA processing, the beamwidth should be independent of the depth.

In Fig. 6, the beamwidth of the main lobe versus depth is plotted for data processed with the four apodization weights for the 20-MHz transducer. The plot of the results for the boxcar window for the 20-MHz transducer shows that SA processing can achieve better focusing than the actual focus of the transducer. This can happen if the ratio of the synthetic aperture to the desired focal depth were greater than the ratio of the transducer's diameter to its focal depth. The difference in beamwidth is actually only 27 μm. The wire is 25 μm in diameter. The results for the 15-MHz transducer are similar with slightly greater beamwidths. These beamwidths should be compared to the beamwidths at the focus of each transducer, which are found to be 157 and 159 μm for the 15- and 20-MHz transducers, respectively. The 15-MHz transducer has a larger aperture angle, so it can achieve a larger synthetic aperture, but the images produced with the 20-MHz transducer had better resolution due to the smaller wavelength and the fact that not all of the potential subaperture of the 15-MHz transducer was used to reduce computational complexity.

The lateral resolution is degraded by the use of apodization weights; however, they are still used to lower the sidelobes in the beam pattern. Four beam patterns for the four different windows studied are shown in Fig. 7 for the wire

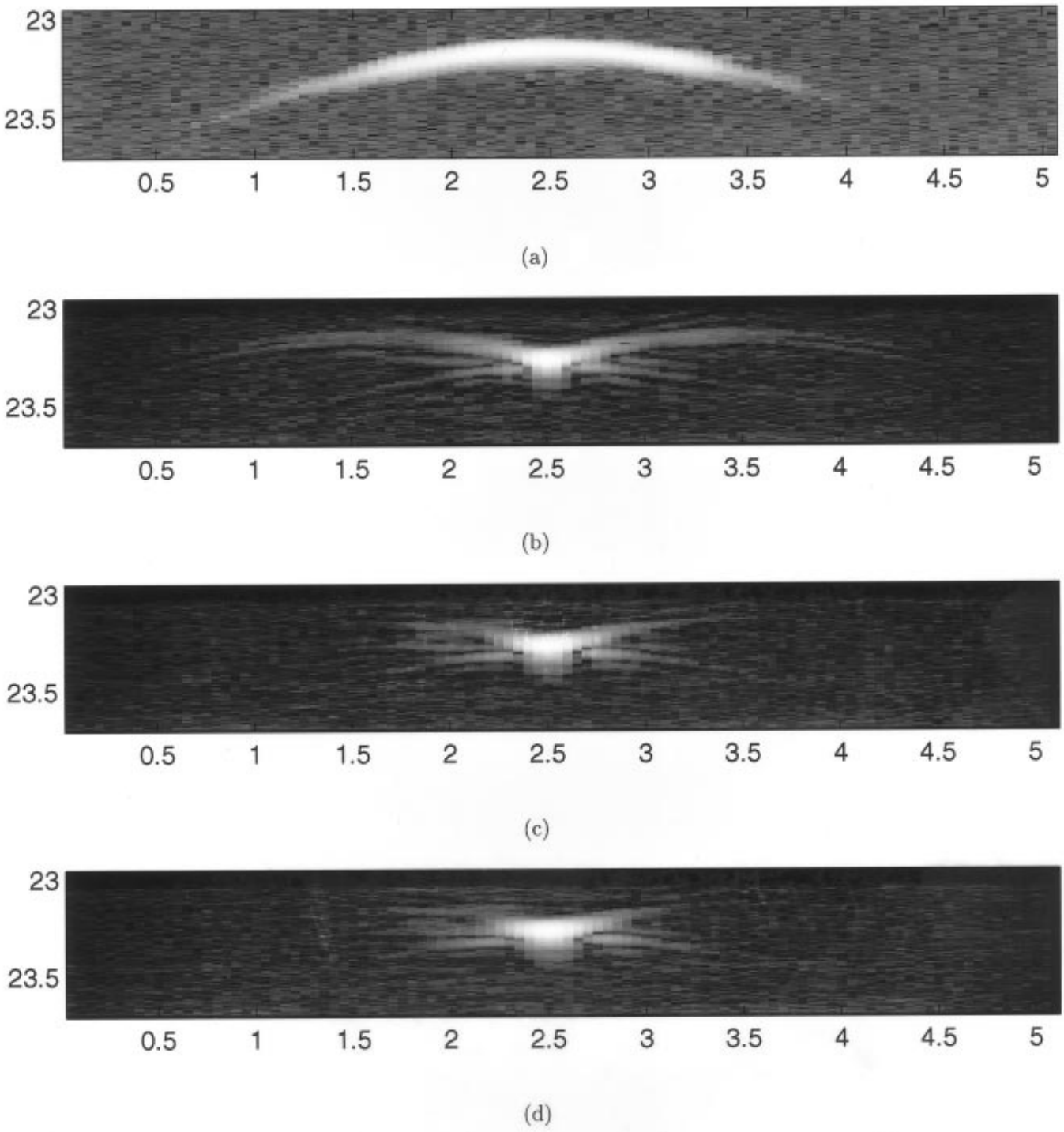

Fig. 4. Images produced with synthetic aperture processing displayed over a 50-dB range. All axes are labeled in millimeters. The data are collected in a degassed waterbath using the 15-MHz transducer with the tungsten wire positioned 5 mm beyond the focus: (a) Raw data, (b) synthetic aperture processing using boxcar apodization weights, (c) cosine apodization weights, and (d) Hamming apodization weights.

TABLE II
BEAMWIDTHS AND SIDELOBE LEVELS FOR TUNGSTEN WIRE DATA.

Resolution and Sidelobe Levels for Tungsten Wires in Degassed Water							
		15 MHz			20 MHz		
Wire depth (mm)		3	5	7	3	5	7
6-dB Beamwidth (μm)							
	raw data	525	1451	2117	863	1740	2349
	boxcar	189	184	215	143	132	161
	cosine	212	219	263	168	169	202
	triangle	222	234	287	182	184	219
	Hamming	227	242	298	188	191	229
Sidelobe level (dB)							
	raw data	−26.0	−15.9	−11.9	−22.3	−12.1	−10.4
	boxcar	−29.4	−26.6	−25.7	−25.0	−22.1	−15.8
	cosine	−34.0	−27.5	−28.9	−26.9	−28.6	−18.9
	triangle	−34.3	−30.1	−34.5	−28.7	−29.1	−22.1
	Hamming	−37.1	−28.7	−29.9	−21.4	−23.0	−20.0

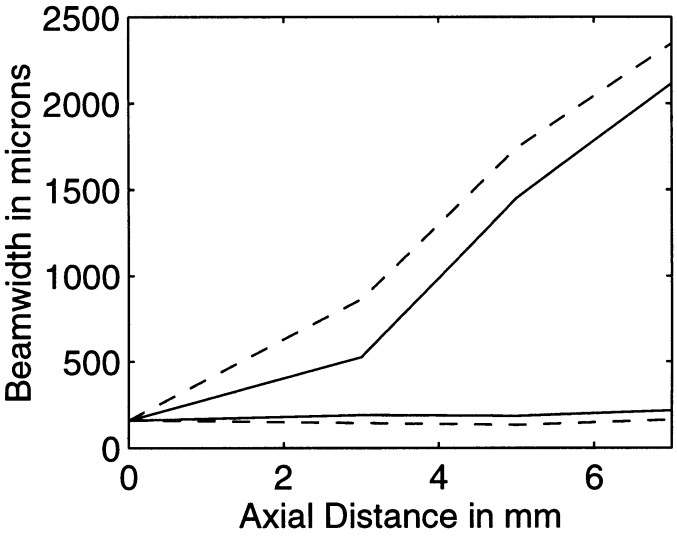

Fig. 5. Comparison of 6-dB beamwidth versus depth for the tungsten wire in a degassed waterbath before and after SA processing for the 15-MHz (solid lines) and 20-MHz (dashed lines) transducers. The plot of beamwidth before processing for each transducer has the large slope. The plot of beamwidth after SA processing for each transducer is almost horizontal.

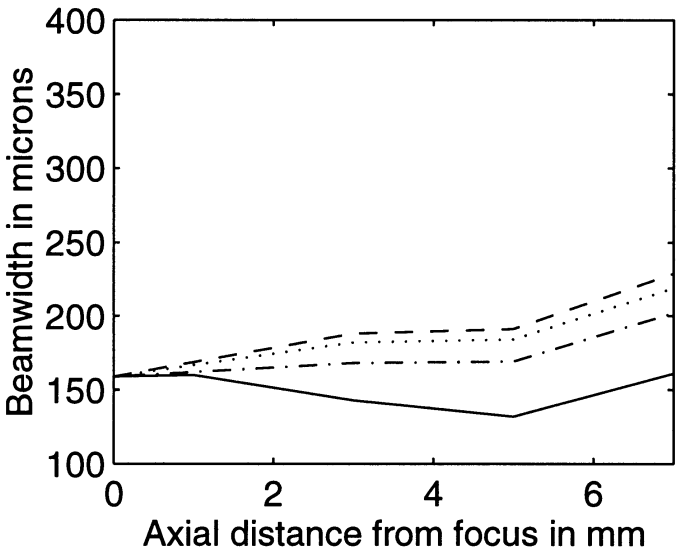

Fig. 6. Comparison of 6-dB beamwidth versus depth after SA processing with boxcar (solid line), triangle (dotted line), cosine (dot-dashed line), and Hamming (dashed line) apodization weights for the 20-MHz transducer with a tungsten wire target in a degassed waterbath.

at depth 3 mm from the focus using the 20-MHz transducer. The use of nonuniform weights lowered the sidelobes as can be seen from the beam patterns and the data in Table II. The improvement is also clear from the images shown in Fig. 4. The cosine and triangle apodization weights produce images that compromise between the best lateral resolution and lowest sidelobe level.

The beamwidths calculated from the tissue-mimicking phantom data processed with uniform weights are displayed in Table III. The 6-dB transmit-receive beamwidth is the smallest for the most shallow wire but remains nearly constant over the deeper range in the image. The wires actually have a width of 120 μm. The modified lateral resolutions for the tissue-mimicking phantom processed with apodization weights are also listed in Table III. The results are similar to the tungsten wire data results, in that

TABLE III
RESOLUTION OF 120-μM WIRE TARGETS IN TISSUE-MIMICKING PHANTOM IN IMAGES PRODUCED WITH UNIFORM AND NONUNIFORM WEIGHTS. RF DATA ARE COLLECTED WITH A 15-MHZ TRANSDUCER.

Resolution of Wires in Tissue Phantom					
Wire depth in phantom (mm)		7	8	9	10
6-dB Beamwidth (μm)					
	raw data	1632	1866	2244	2385
	boxcar	495	536	580	568
	cosine	588	655	718	721
	triangle	632	693	762	784
	Hamming	694	812	823	825

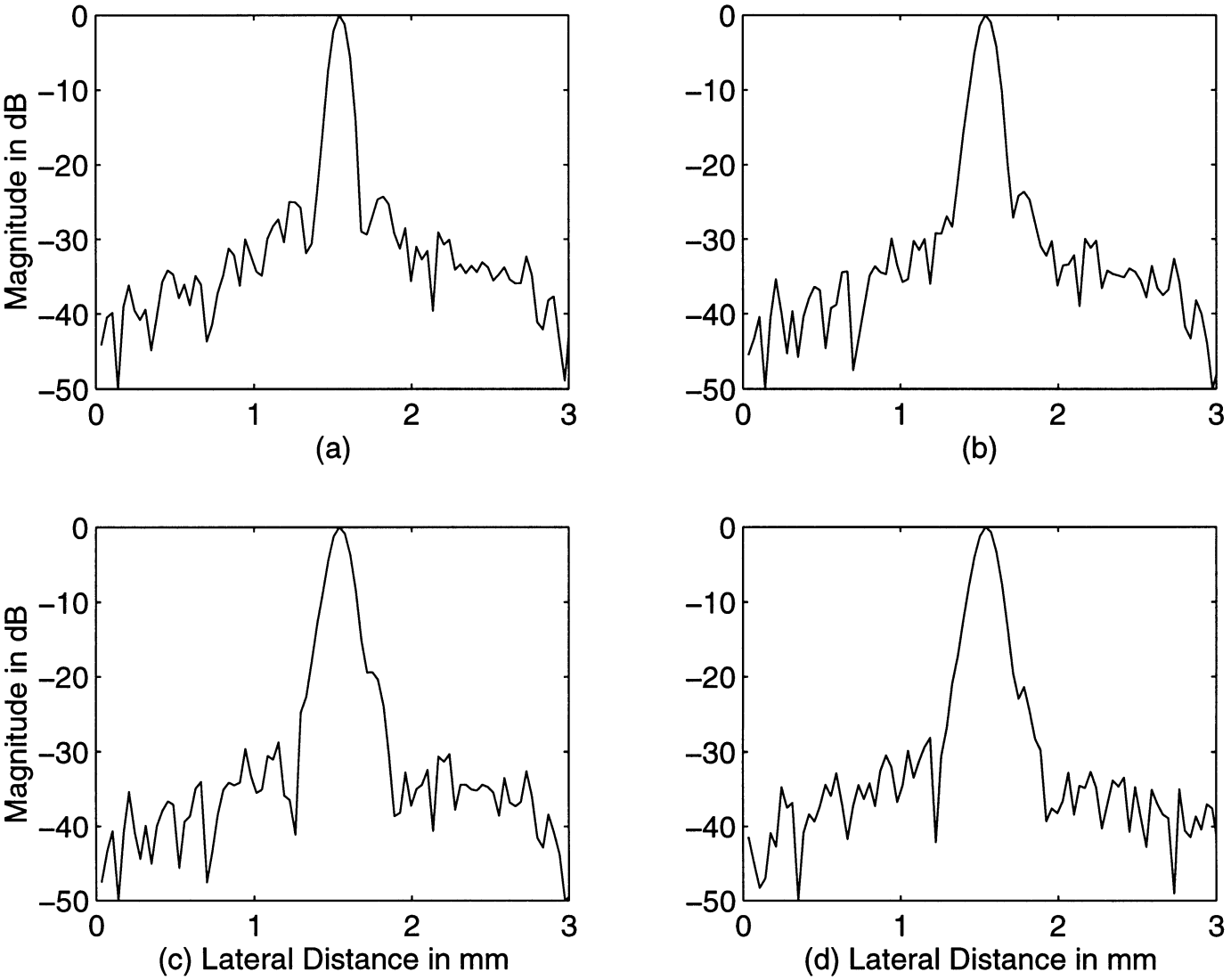

Fig. 7. Beamplot at wire using (a) boxcar, (b) cosine, (c) triangle, and (d) Hamming apodization weights to produce images from the data collected with the 20-MHz transducer with the tungsten wire positioned 3 mm beyond the focus.

the wire beam widths increase after processing with the windows. The Hamming window forces a greater increase in the beamwidth than the other two.

Cyst data are also used to compare the performance of processing with a boxcar window and processing with other windows. The amount of cyst fill-in gives a qualitative measure of the main lobe beamwidths and the sidelobe levels. Images produced using uniform and nonuniform weights are shown in Fig. 8. In order to quantify the quality of these images, a contrast-to-noise ratio (CNR) is calculated for each target [7], that is,

$$\mathrm{CNR} = \frac{|\mu_c - \mu_b|}{\sigma_b} \tag{7}$$

where μ_c is the mean intensity of the cyst in dB, μ_b is the mean of the background, and σ_b is the standard deviation of the background. As expected, the CNR is greater for the larger cyst than for the smaller one, because it is easier to isolate a large cyst in the main lobe of a beam than a small one. Quantitative values of CNR are presented in Table IV for the boxcar window and the other windows. The images produced by processing with nonuniform weights performed better than the boxcar window due to the lower sidelobes. Again, the CNR for the cosine and triangle weights are similar; the cosine weights had a slightly better CNR due to the more narrow beam. The Hamming weights do not improve the CNR over the other two windows because the beamwidth is too large and the sidelobes are not appreciably lower.

B. Appearance of Grating Lobes Versus Spatial Sampling

In order to test the necessity of collecting signals from transducer positions located less than half a wavelength apart, the tungsten wire data collected 20 μm apart for the wire located 8 mm beyond the focus are decimated in the lateral direction. Images are produced with spatial sampling of $\frac{2\lambda}{5}$, $\frac{3\lambda}{5}$, λ, $\frac{7\lambda}{5}$, and 2λ, corresponding to lateral decimation factors of 2, 3, 5, 7, and 10.

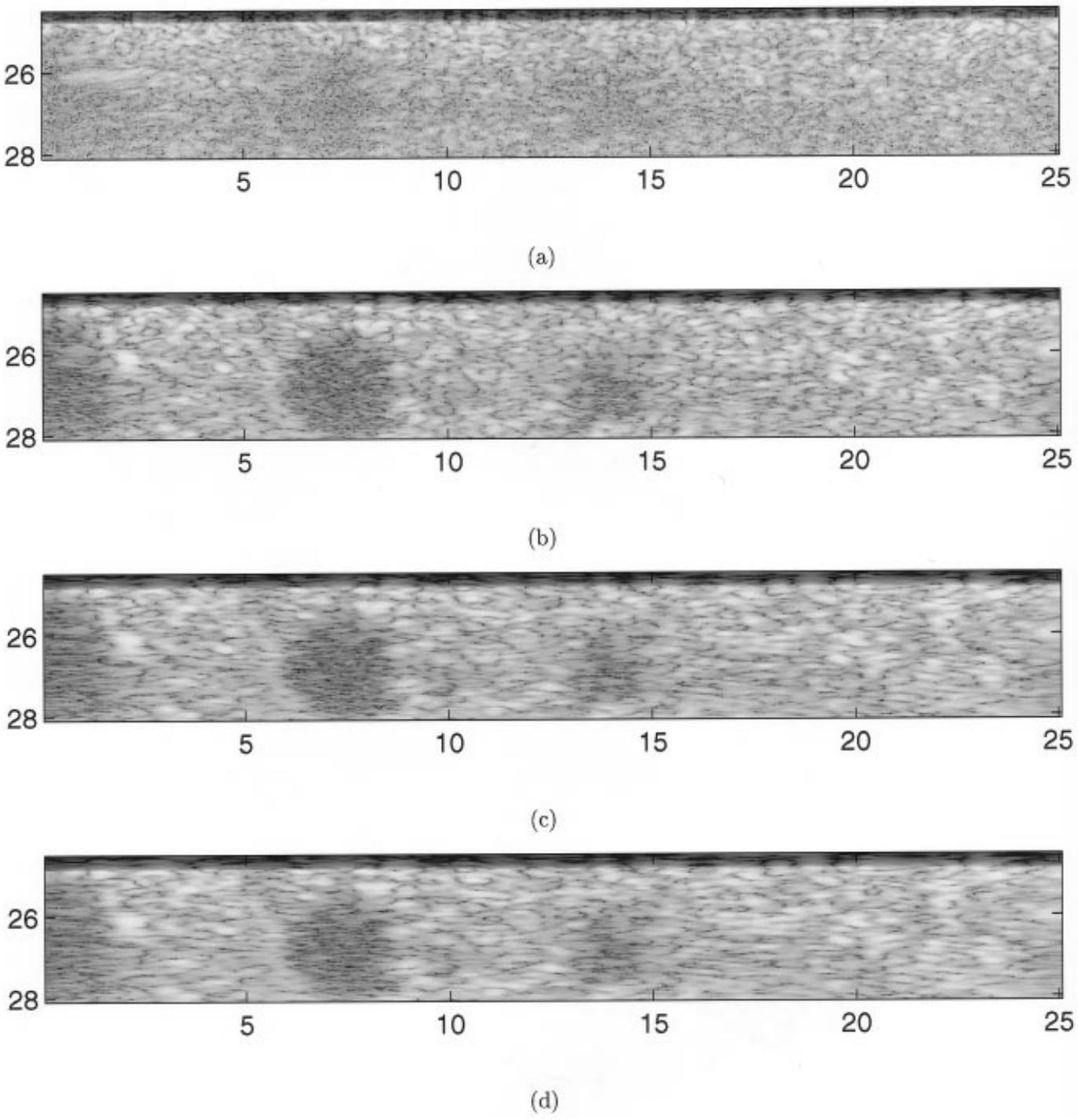

Fig. 8. Images produced from cyst data with synthetic aperture processing displayed over a 50-dB range. The data are collected using the 15-MHz transducer. (a) Raw data, (b) synthetic aperture processing using boxcar apodization weights, (c) cosine apodization weights, (d) Hamming apodization weights.

TABLE IV
SNR CHARACTERISTICS OF THE RF DATA FOR 25-μM TUNGSTEN WIRE TARGETS IN A WATERBATH. MEAS. RF SIGNAL SNR REFERS TO THE SNR OF A SIGNAL RECEIVED BY THE TRANSDUCER AT A GIVEN POSITION. CALC. RF SIGNAL SNR REFERS TO THE SNR OF THE PROCESSED RF SIGNAL. DATA ARE PROCESSED WITH THE BOXCAR WINDOW.

SNR of RF Data					
Tdr (MHz)	Wire depth (mm)	Ideal SNR improvement (dB)	Meas. RF signal SNR (dB)	Calc. RF signal SNR (dB)	Meas. SNR improvement (dB)
15	0	–	64.46	–	–
	3	13.22	44.73	51.52	6.79
	5	15.91	38.93	47.17	8.24
	7	17.56	36.33	60.92	24.59
20	0	–	50.37	–	–
	3	16.13	33.70	46.98	13.28
	5	17.85	25.56	38.49	12.93
	7	19.40	24.84	49.56	24.72

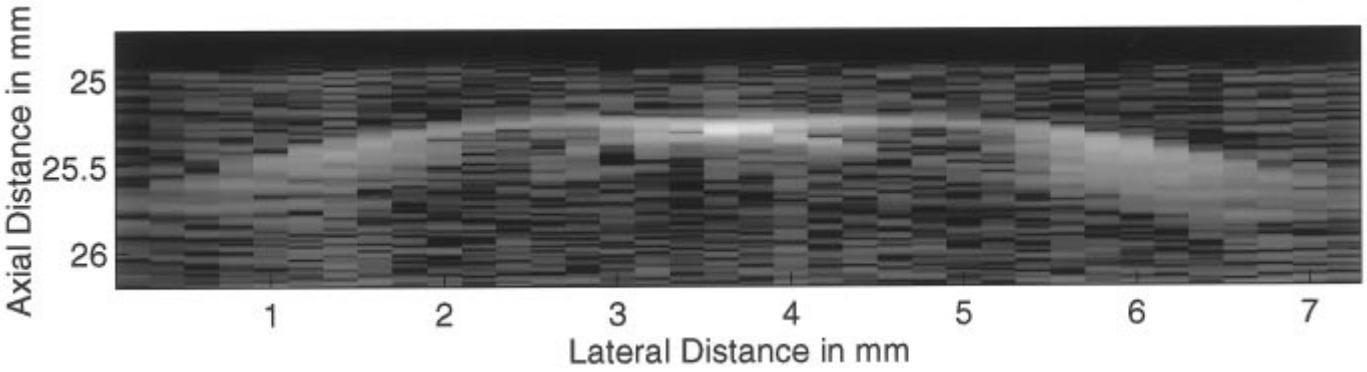

Fig. 9. Grating lobes that appear when RF data are collected two wavelengths apart. Data are collected using the 15-MHz transducer with the tungsten wire target positioned 8 mm beyond the focus. The image is displayed over a 50-dB range.

No grating lobes are found for data sets sampled at $\frac{2\lambda}{5}$, $\frac{3\lambda}{5}$, or λ. Grating lobes are not expected for the image sampled at $\frac{2\lambda}{5}$ because the spatial sampling is still less than half of a wavelength. Even sampling the data at $\frac{3\lambda}{5}$ gives a sampling rate close to the half wavelength limit.

From (3), grating lobes that exist when the data are sampled one wavelength apart would appear at $\theta = 30$ and 90 degrees. Here, no change in the image is expected from the grating lobes at 90 degrees because there is no target at this location to interfere in the image. However, it would be possible to see a response from a grating lobe that appears at 30 degrees. Because the virtual source has a limited aperture angle, the grating lobe at 30 degrees is expected to be down by 22.4 dB. Also, there is a reduction in the size of grating lobes because the image is created with a pulse rather than a continuous wave. The minimum number of elements used to create a block of the image is 17. The pulse has a length of less than two wavelengths. This corresponds to a reduction of 15.0 dB. Finally, there is an additional reduction in grating lobe strength because the pulse is not coherent. Therefore, even though grating lobes may exist, they do not rise above the noise level in this image.

Grating lobes are observed for the images created from the data decimated by factors of 7 and 10 corresponding to lateral sampling of $\frac{7\lambda}{5}$ and 2λ. In the image decimated by 7, the measured grating lobe has a magnitude 18.9 dB below that of the main lobe. It is located at 17.9 degrees. There, the reduction due to the directivity of the beam is 7.4 dB, and the reduction due to the pulsed waveform is 12.7 dB for a total level of -20.1 dB. Further reduction in magnitude occurs because the pulse is not a single frequency; so, even when the pulses from neighboring elements do overlap, they do not overlap exactly. This effect causes the grating lobe to broaden and be lower in magnitude.

TABLE V
CONTRAST-TO-NOISE RATIO FOR CYST TARGETS IN IMAGES PRODUCED WITH UNIFORM AND NONUNIFORM APODIZATION WEIGHTS. RF DATA ARE COLLECTED WITH A 15-MHZ TRANSDUCER.

Contrast to Noise Ratios		
Window	2 mm cyst (dB)	3 mm cyst (dB)
raw data	1.11 ± 0.32	1.01 ± 0.33
boxcar	1.59 ± 0.25	1.84 ± 0.24
cosine	1.70 ± 0.21	1.99 ± 0.21
triangle	1.78 ± 0.19	2.08 ± 0.19
Hamming	1.71 ± 0.17	2.01 ± 0.17

For the image decimated by a factor of 10, the grating lobes are observed at 14.3 degrees. The image with the grating lobes is shown in Fig. 9. The grating lobes have an average magnitude of 15.7 dB below the main lobe. At this angle, the reduction due to the limited beam is 3.1 dB, and the reduction due to the pulse length is 9.5 dB for a total reduction of 12.6 dB. Again the grating lobes are smeared, because of lack of coherence in the pulse contributing to total measured reduction.

These results demonstrate that spatial sampling rate can be less than the $\frac{\lambda}{2}$ limit without the appearance of grating lobes.

C. SNR Results

Electronic SNRs are calculated for individual pulse-echo RF returns and image SNRs are calculated for the images formed with boxcar apodization weights. The image SNR is calculated as in [7] using the image data before logarithmic compression. A value for the signal is measured as the rms pixel value in a small rectangle over the wire in the image. The noise value is taken as the average rms pixel value in four rectangles located where there is no signal or sidelobe contribution. The SNR is then the ratio of the signal to noise expressed in dB.

Assuming uncorrelated, additive electronic noise, the SNR of the processed RF signal would ideally show an improvement over that of a measured pulse-echo RF return of $10\log_{10}(L)$ where L is the number of signals included in the sum to create a single RF signal for the image. The results of these measurements and calculations are shown in Table V. The value in the table given for the measured pulse-echo RF return is the median value for the SNR of all the RF returns included in the sum to get the calculated RF signal whose SNR is listed in the next column of the table. The SNR showed less than the ideal improvement, which results from quantization errors in the delays and the range of SNRs for the included pulse-echo RF returns. Received signals show a larger SNR when the wire is near the center of the beam than when the wire is at the edge of the beam. The image SNR is listed in Table VI. With a 40-dB receiver gain, the SNR is 34.1 dB on average. The SNR is higher for the 15-MHz transducer than for the 20-MHz transducer due to the bandwidth of the transmitted pulse. The same experiment is repeated using 20-dB gain to amplify the RF signal, which produced an SNR of 19.7 dB on average.

The two transducers show different improvement because more elements are included in the sum for the 20-MHz transducer. This transducer actually has a smaller beam spread, which would seem to indicate summing fewer RF signals, but the transducer positions were closer together because of the smaller wavelength.

SA processing improves both the SNR of individual RF signals and the SNR of the image when the wire is located beyond the focus of the transducer. However, the processing does not improve either SNR above the level acheived when the target is located at the focus of the transducer. The SNR of a measured RF signal from a wire at the focus of the transducer is only slightly higher than the SNR of a calculated RF signal when the target is 7 mm away and a relatively large number of measured RF signals are summed. Similarly, the SNR of a calculated RF signal from a wire target 3 mm from the focus can be high because it is so close to the focus, even though relatively few measured RF signals are summed. In the intermediate range, the electronic SNR is not as good as that obtained when the target is at the focus of the transducer. The image SNR is also improved greatly through SA processing. And it shows a similar trend as the electronic SNR, coming close to the image SNR for a B-mode image when the wire is at the focus when the wire is at 3 mm or 7 mm. When the wire is at 5 mm, the image SNR is not as good as the image SNR for the conventional B-mode image when the wire is at the focus.

TABLE VI
SNR CHARACTERISTICS OF THE PROCESSED IMAGES OF 25-μM TUNGSTEN WIRE TARGETS IN A WATERBATH. DATA ARE PROCESSED WITH THE BOXCAR WINDOW.

		SNR of Images	
Tdr (MHz)	Wire depth (mm)	Unprocessed image SNR (dB)	Processed image SNR (dB)
15	0	38.6	–
	3	33.18 ± 0.45	32.76 ± 1.50
	5	23.24 ± 0.31	35.31 ± 1.05
	7	21.39 ± 0.34	38.05 ± 0.50
20	0	31.9	–
	3	23.89 ± 0.36	30.01 ± 0.78
	5	15.57 ± 0.39	28.89 ± 0.95
	7	15.18 ± 0.19	34.98 ± 1.14

VI. Conclusion

The behavior of a virtual source in response to synthetic aperture processing has been studied. The results show that it is possible to treat the focus of a transducer as a virtual element for the sake of SA processing. Once the aperture angle of the transducer has been determined, SA processing can be performed without regard to whether or not the element actually exists.

Using SA processing, resolution beyond the focus of the transducer is improved. The minimum lateral resolution achievable is limited by the diffraction angle of the transducer. However, we have shown that the achievable resolution can be comparable to the resolution at the focus of the transducer.

The tradeoff between resolution and sidelobe level is demonstrated for wire and cyst targets. As with any engineering compromise, the best images are produced with the apodization weights that do not achieve the best resolution or lowest sidelobe level but rather compromise between the two.

The spatial sampling criterion is investigated by forming images with decreasing sampling rates. The accepted criterion is shown to be more strict than actually necessary. Therefore, the amount of computation can be reduced by working beyond the $\frac{\lambda}{2}$ limit, but not so far that grating lobes are observed.

The image SNR can be close to the SNR for an image created with conventional B-mode imaging with the target at the focus. And the image SNR is improved compared to conventional B-mode imaging when the target is beyond the focus.

One issue in SA imaging that has not been discussed in this contribution is the problem of phase aberration caused by spatial variations of the speed of sound, which occur in biological tissue. Tissue inhomogeneity also affects conventional B-mode images by increasing the size of the focal spot. With the virtual source technique, the increase in size of the focal spot is not a problem unless the diffraction angle is also reduced. However, tissue inhomogeneity will cause errors in the calculation of delays. This problem has limited the use of SA processing in medical imaging, but many groups are currently working on methods to reduce its effects on SA images. And SA is well-established in other applications such as nondestructive evaluation.

References

[1] C. Passman and H. Ermert, "A 100 MHz ultrasound imaging system for dermatologic and ophthalmologic diagnostics," *IEEE Trans. Ultrason., Ferroelect., Freq. Contr.*, vol. 43, pp. 545–552, July 1996.

[2] H. Djelouah, J. C. Baboux, and M. Perdrix, "Theoretical and experimental study of the field radiated by ultrasonic focussed transducers," *Ultrasonics*, vol. 29, pp. 188–200, May 1991.

[3] K. Raum and W. D. O'Brien, Jr., "Pulse-echo field distribution measurement technique for high-frequency ultrasound sources," *IEEE Trans. Ultrason., Ferroelect., Freq. Contr.*, vol. 44, pp. 810–815, July 1997.

[4] J. G. Proakis and D. G. Manolakis, *Digital Signal Processing: Principles, Algorithms, and Applications*. New York: MacMillan, 1992.

[5] O. T. von Ramm and S. W. Smith, "Beam steering with linear arrays," *IEEE Trans. Biomed. Eng.*, vol. BME-30, pp. 438–452, Aug. 1983.

[6] M. O'Donnell, B. M. Shapo, M. J. Eberle, and D. N. Stephens, "Experimental studies on an efficient catheter array imaging system," *Ultrason. Imaging*, vol. 17, pp. 83–94, 1995.

[7] M. Karaman, P.-C. Li, and M. O'Donnell, "Synthetic aperture imaging for small scale systems," *IEEE Trans. Biomed. Eng.*, vol. 42, pp. 429–442, May 1995.

[8] J. T. Ylitalo and H. Ermert, "Ultrasound synthetic aperture imaging: Monostatic approach," *IEEE Trans. Ultrason., Ferroelect., Freq. Contr.*, vol. 41, pp. 333–339, May 1994.

Catherine Frazier (S'97) was born on August 16, 1972, in Bethesda, MD. She received the B.S.E.E. from the University of Maryland at College Park in 1994, and the M.S. in electrical engineering from the University of Illinois at Urbana-Champaign in 1996. She is currently working on the Ph.D. in electrical engineering at the University of Illinois.

Ms. Frazier was awarded the National Science Foundation Fellowship from 1994 to 1997, and the Koehler Fellowship for the 1994–1995 academic year. In April 1997 she was presented the Robert T. Chien Memorial Award for outstanding research in electrical engineering.

Her research interests are in acoustical image formation and image processing.

William D. O'Brien, Jr. (S'64–M'71–SM'79–F'89) received B.S., M.S., and Ph.D. degrees in 1966, 1968, and 1970, from the University of Illinois, Urbana-Champaign.

From 1971 to 1975 he worked with the Bureau of Radiological Health (currently the Center for Devices and Radiological Health) of the U.S. Food and Drug Administration. Since 1975, he has been at the University of Illinois, where he is a Professor of Electrical and Computer Engineering and of Bioengineering, College of Engineering, and Professor of Bioengineering, College of Medicine, is the Director of the Bioacoustics Research Laboratory and is the Program Director of the NIH Radiation Biophysics and Bioengineering in Oncology Training Program. His research interests involve the many areas of ultrasound-tissue interaction, including spectroscopy, risk assessment, biological effects, tissue characterization, dosimetry, blood-flow measurements, acoustic microscopy and meat characterization for which he has published more than 170 papers.

Dr. O'Brien is Editor-in-Chief of the *IEEE Transactions on Ultrasonics, Ferroelectrics, and Frequency Control*. He is a Fellow of the Institute of Electrical and Electronics Engineers (IEEE), the Acoustical Society of America (ASA), and the American Institute of Ultrasound in Medicine (AIUM) and a Founding Fellow of the American Institute of Medical and Biological Engineering. He was recipient of the IEEE Centennial Medal (1984), the AIUM Presidential Recognition Awards (1985 and 1992), the AIUM/WFUMB Pioneer Award (1988), the IEEE Outstanding Student Branch Counselor Award (1989), and the AIUM Joseph H. Holmes Basic Science Pioneer Award (1993). He has been President (1982–1983) of the IEEE Sonics and Ultrasonics Group (currently the IEEE UFFC-Society), Co-Chairman of the 1981 IEEE Ultrasonic Symposium, and General Chairman of the 1988 IEEE Ultrasonics Symposium. He has also been President of the AIUM (1988–1991) and Treasurer of the World Federation for Ultrasound in Medicine and Biology (1991–1994).